

EMC Society of Australia

NEWSLETTER

JUNE 2020, ISSUE 89



AUSTRALIAN-DESIGNED AI ATTACK DRONE PROTOTYPE UNVEILED BY BOEING AHEAD OF MASS PRODUCTION

From ABC Defence correspondent Andrew Greene

An Australian-designed military drone that uses artificial intelligence technology to target enemies has been unveiled to the public, the first military plane to be designed and built locally in more than half a century. Developed by the Royal Australian Air Force (RAAF) and US manufacturer Boeing, the Loyal Wingman drone has a range of 3,700 kilometres and is expected to eventually join manned aircraft such as Joint Strike Fighters into battle.

The working prototype of the Loyal Wingman unveiled today will now begin ground testing, with taxi tests and flight tests due later this year. The Federal Government has contributed \$40 million towards the historic and secretive project. Prime Minister Scott Morrison hailed the aircraft's development as a "truly historic moment for our country and for Australian defence innovation".

"The Loyal Wingman will be pivotal to exploring the critical capabilities our Air Force needs to protect our nation and its allies into the future," Mr Morrison said in a video message released at today's unveiling.

Air Force Chief Air Marshal Mel Hupfeld said the rollout of the first aircraft was a significant milestone in the Boeing Loyal Wingman project. "This project is an excellent example of innovation through collaboration and what can be achieved working together with defence industry," Air Marshal Hupfeld said.

The RAAF plans to buy three drones, which Boeing calls the Airpower Teaming System (ATS), as part of the Loyal Wingman Advanced Development Program. ATS uses artificial intelligence to complement and extend missions flown by traditional combat aircraft.

Mass production of the unmanned jet fighter is likely to begin by the middle of the decade.

"We are expecting middle of the decade, maybe a bit earlier, that this will be in production," Boeing's Shane Arnott said.



IEEE

A joint publication of the EMC Society of Australia (Engineers Aust.)
and the Victorian (Aust.) Chapter of IEEE EMC Society

www.engineersaustralia.org.au/emcsa

Engineers Australia 11 National Circuit, Barton ACT 2600

EMC SOCIETY NATIONAL COUNCIL

The EMC Society is a Technical and learned society within Engineers Australia, established to promote the science and practice of Electromagnetic Compatibility through Australia and the region.

NATIONAL COUNCIL

Chairman & Website Liaison ~ Mark Mifsud

Treasurer & Vice Chair ~ Kingsley McRae

Member Co-ordinator ~ Paul Payne

Secretary & Newsletter Editor EMCSA Newsletter ~ Steve Offer

New South Wales Representative ~ Steve Brine

South Australian Representative ~ Arthur Weedon

Sub-editor EMCSA Newsletter ~ Daniel Liu

Sub-editor EMCSA Newsletter ~ Hong Mei Fan

PORTFOLIOS

Newsletter

Steve Offer, Daniel Liu,
Hong Mei Fan

Webmaster

Arthur Weedon

Publicity and IEEE Liaison:

Mark Mifsud

Membership

Paul Payne

<http://www.engineersaustralia.org.au/emcsa>

CONTENTS

03 CHAIRMAN'S
MESSAGE

04 WORKSHOP
REVIEWS

05 VARIOUS
PAPERS

16 STANDARDS
UPDATE

18 IN THE
AETHER

19 INSTITUTIONAL
LISTINGS

The opinions, comments, endorsements, and other such information provided herein are not those of the EMC Society of Australia, Engineers Australia or the IEEE, they are solely the opinion of the authors.

Chairman's Message

JUNE 2020

As I compile my message to our members, in self isolation, I reflect on the fact that I should have been hosting APEMC 2020 this week. I am a great believer that fate determined that it was not meant to be. What would have been worse would be the responsibility of the health of attendees if we weren't aware that COVID-19 was spreading world wide. Fate does work in strange ways.

Australia in the main has dodged a bullet, at the moment at least. With adversity comes opportunity and with some concerted effort by the committee we have been able to secure some quality speakers to provide live webinars for our members.

This will enable members all over the country to participate and have the ability to ask the presenter question during the webinar. Engineers Australia will provide this service via Webex Events.

Our first confirmed speaker is Dr. Farhad Rashidi who currently resides in Switzerland. Farhad is well regarded in the international EMC community and was recommended by the current IEEE EMC Society President, Professor Alistair Duffy.

The presentation is titled "An Introduction to Electromagnetic Time Reversal and its Applications to EMC."

The presentations is to be held on the 23 July at 6:30pm.

Once we have confirmation from Engineers Australia we will provide registration details



on our webpage www.emcsa.org.au and we will email you if you are on our distribution list. Stay tuned for further presentations this year and once it is safe to do so we will endeavour to organise physical events.

Contributions to the newsletter relating to EMC are always welcome. We are endeavouring to provide value for money. Your continued support and feedback are valued.

Contact us at presentations@emcsa.org.au or enquiries@emcsa.org.au.

In the mean time stay safe and be vigilant.

Mark Mifsud
CHAIRMAN



EMC Society
of Australia

IEEE Sister Society
EMC
SOCIETY®

The EMC Society of Australia (EMCSA) is a technical society within the Electrical College of Engineers Australia. It was formed to foster technical exchange on matters related to the branch of electronic engineering known as Electromagnetic Compatibility. The EMCSA is a sister society of the IEEE Electromagnetic Compatibility Society which is the world's largest organization dedicated to the development and distribution of information, tools and techniques for reducing electromagnetic interference. The historical 'Sister Society' signing occurred in 2013, see below.

EMC Society Activities

As the main focal point for EMC in Australia, the EMCSA performs the following functions:

- Participation in Standards Australia Technical Committees TE-003 (Electromagnetic Compatibility) and RC-006 (Radiocommunications Equipment).
- Coordination of a annual Australian workshop for EMC;
- Publication of a newsletter;
- Coordination of technical presentations on EMC;

EMC Society Workshop

Our one day annual workshop features short and long presentations from National and International experts in industry and academia, as well as Industry Exhibitions. Upcoming workshop details are available at : <http://www.emcsaworkshop.org.au/>.



EMC Newsletter

The EMC Newsletter is a joint publication of the EMC Society of Australia and the Victoria Chapter of the IEEE EMC Society. View our latest editions by clicking on the links below. Past editions are available in our web site.

Join the EMC Society

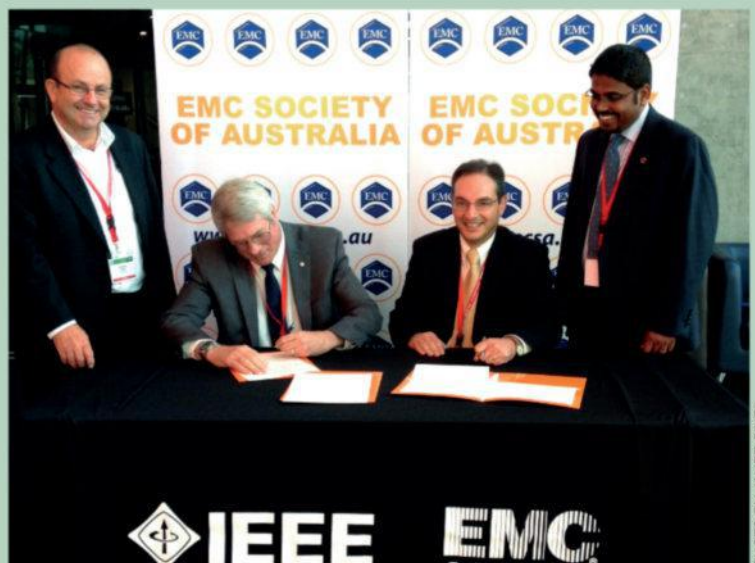
Membership of the EMC Society of Australia is open to individuals and corporations having an interest in EMC. Student membership is free. Simply complete and submit the form at <http://www.engineersaustralia.org.au/emcsa/>.

Sister Society Agreement Signed in Australia

By Vignesh Rajamani, IEEE EMC Society Sister Society Coordinator

As part of the growing Sister Society efforts, the IEEE EMC Society recently signed the Sister Society agreement with the EMC Society of Australia (EMCSA) during the 2013 Asia Pacific EMC Symposium in Melbourne, Australia. This historic agreement between the two societies enables all the EMCSA members to be recognized as a Sister Society member of the IEEE EMC Society.

Through the Sister Society Agreements, possible collaboration in the areas of membership, publications, technical meetings, and various joint activities are promoted. The EMC Society will make available IEEE Affiliate Membership to the members from other societies with whom we have Sister Society Agreements, which provides many of the same privileges as EMC Society members enjoy for publications, subscriptions, access to EMC Society on-line publications, and technical activities. In addition, technical meetings will benefit from co-sponsorship and cross promotion of conferences, symposia and workshops, and the mutual granting of registration discounts.



The formal signing of the "Sister Society" agreement between the EMC Society of Australia and the IEEE EMC Society took place in Melbourne during the AP EMC 2013 Symposium. Shown from left are Kingsley McRae of the EMC Society of Australia; Ghery Pettit, IEEE EMC Society President; Mark Mifsud, Chair of the EMC Society of Australia; and Vignesh Rajamani, IEEE EMC Sister Society Coordinator.

PHOTO BY JANET O'NEIL

Analysis and Design of Coil-Based Electromagnetic-Induced Thermoacoustic for Rail Internal-Flaw Inspection

Wensong Wang, Zilian Qu, Zesheng Zheng, Song Yong Phua, Kelvin, Christian Ivan, Kye Yak See, *Senior Member, IEEE*, and Yuanjin Zheng, *Senior Member, IEEE*

Abstract—A novel coil-based electromagnetic-induced thermoacoustic system is presented for detecting the flaws inside the rail. The fundamental is derived and thus the overall energy density distribution is simulated using finite element method. This paper gives an overview of the system architecture and describes in detail the design process. A mixed numerical experimental methodology is employed to extract the lumped parameters of a planar coil with the ferrite plate for designing the matching network, and then the coil and rail are co-simulated to observe the current density distributions and directions. Through the relationship of energy density and depth in the rail, it is found that the thermal energy mainly concentrates at the surface local area. From the interaction between the coil and rail, the inductive power transfer topology is illustrated and the simplified equivalent circuit model is further obtained. By analyzing the simulated and measured data, the changes of the resistance and inductance are shown with the frequency increasing. The induced ultrasonic wave propagation is simulated inside the rail with flaws, where the wavefronts and reflected signals are observed. Finally, experimental results demonstrate the proposed design is feasible and the crack with the diameter of 8 mm can be detected in the rail.

Index Terms—Rail internal-flaw inspection, planar stranded coil, electromagnetic-induced thermoacoustic, equivalent circuit model, multiphysics.

I. INTRODUCTION

ULTRASOUND based methods have been studied to inspect and evaluate internal flaws in the metallic products and other mechanical structures because of the efficient propagation and high safety for human [1]–[2]. However, the traditional acoustic coupling between the piezoelectric transducer and a

Manuscript received June 17, 2018; revised October 08, 2018; accepted November 14, 2018. (*Corresponding author: Wensong Wang.*)

W. Wang, Z. Zheng, K. Y. See and Y. Zheng are with the School of Electrical and Electronic Engineering, Nanyang Technological University, Singapore 639798 (e-mail: uscnuaa@gmail.com; zesheng001@e.ntu.edu.sg; ekyysee@ntu.edu.sg; yjzheng@ntu.edu.sg).

Z. Qu was with the School of Electrical and Electronic Engineering, Nanyang Technological University, Singapore 639798. He is now with the Beijing Information Technology College, Beijing 100015, China (e-mail: zilian_qu@163.com).

S. Y. Phua, Kelvin and C. Ivan are with the SMRT Trains Pte Ltd, Singapore (e-mail: PhuaSongYongKelvin@smrt.com.sg; IvanChris@smrt.com.sg)

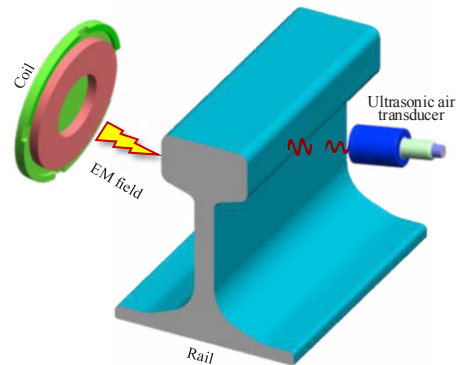


Fig. 1. Proposed rail internal-flaw inspection scheme.

tested specimen is difficult or challenging to be implemented in many special environments such as hot/cold, complex-shaped, and fast-moving, since the coupling fluid is an indispensable part in the method.

Thus, non-destructive test techniques are developed such as photoacoustic (PA) and electromagnetic acoustic transducer (EMAT). For the EMAT, a high-density permanent magnet is needed to provide the bias magnetic field for producing longitudinal waves and is hard to fix [3]–[4]. The PA technique is realized by modulating heat on the specimen under a safe level, which can create the acoustic waves by means of the thermal expansion mechanism. Since it was first demonstrated by Alexander Graham Bell in 1880, when he used a pulsed light source to obtain the weak acoustic waves [5], the PA imaging began to be extensively applied for capturing high-quality images of the vasculature [6]–[8]. Then, the laser-based ultrasonic transducer was employed to generate the high-frequency ultrasonic waves on the metal from a large distance [9]–[10]. However, the laser is not only sensitive to the environment like dust and vibration but also has a high cost. Motivated by the development of a low-cost and portable imaging tool for diagnostics and screening, the thermoacoustic (TA) was proposed as PA alternative to improve penetration depth by replacing the laser excitation with the microwave heating [11]–[13]. By far, the low-power microwave heating is mainly applied in the biological research, where the current flows are caused/induced in the material by utilizing electric and magnetic fields [14].

For the materials with high conductivity like iron, aluminum, and other metals, the inductive power transfer (IPT) technology is very efficient for heating [15]. It utilizes the magnetic field as the medium of transferring power and the coil is considered to be the effective radiator in the transmitter, while there is no conventional receiving coil. The IPT is also extensively applied in the vehicle charging [16], bioelectronics microdevices [17], wireless sensor tag [18], etc. To increase the distance between rail and transmitter, this paper also adopts the IPT technology. Periodic heating leads to the stress generation and makes the particles vibrate in the conductive material, termed TA waves.

A coil-based electromagnetic-induced TA technique for the inspection of the flaws in the rail is proposed as shown in Fig. 1. The main contribution of this paper is that the theoretical derivation and experimental verification are conducted, as well as the coil is analyzed and optimized. Compared with other methods of the piezoelectric transducer, EMAT, and PA, this technique can increase the distance between the rail and transmitter, remove the bulky and uncontrollable magnet and be applied in the complex environments. This paper is organized as follows. Section II analytically derives the fundamental theoretical framework and shows the overall system numerical simulation flow. Coupling and conversion effects among the electromagnetism, heat transfer, vibration and ultrasound responses are studied in the complex operating environment using the multiphysics numerical simulations. The detailed system simulations, consisting of a planar coil and parameter extraction, matching network, equivalent circuit model, and ultrasonic wave propagation are performed in Section III. Then, Section IV experimentally validates the system design concept, discloses the physical mechanism for flaw inspection inside the rail, and measures the IPT efficiency and magnetic fields. Finally, Section V draws the conclusion.

II. COIL-BASED ELECTROMAGNETIC-INDUCED TA THEORY

Any conductive material that is exposed to electromagnetic radiation environments will be heated up due to resistive losses. The rapidly time-varying electric and magnetic fields lead to heating sources in the conductive materials since the electric and time-varying magnetic fields can cause/induce current flows, respectively. The coil-based electromagnetic-induced TA mainly utilizes the time-varying magnetic fields radiated from the coil.

The high-frequency alternating current (AC) is passing through the coil and generates the time-varying magnetic field $\mathbf{B}(\mathbf{r})$, which is calculated using the Bio-Savart Law [19]

$$\mathbf{B}(\mathbf{r}) = \frac{\mu_0 N I}{4\pi} \oint_C \frac{d\mathbf{l}' \times (\mathbf{r} - \mathbf{r}')}{|\mathbf{r} - \mathbf{r}'|^3} \quad (1)$$

where C , I , μ_0 , N and $d\mathbf{l}'$ are the whole current path and magnitude of the current flowing through the coil, permeability of free space, number of turns in the coil, and differential coil element, respectively. \mathbf{r} and \mathbf{r}' are the position vectors of the observation point and $d\mathbf{l}'$, respectively.

In presence of the time-varying $\mathbf{B}(\mathbf{r})$, the electromotive force (i.e., voltage) is produced within the conductive material. The magnitude of the induced voltage is proportional to the rate of change of the $\mathbf{B}(\mathbf{r})$ in the given area, and its direction is defined by Lenz's law. The phenomenon can be explained by the

differential form of Faraday's law of induction, i.e., Maxwell-Faraday equation

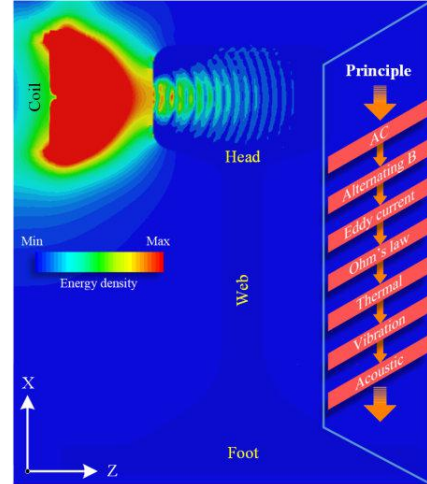


Fig. 2. Energy density distribution extracted by FEM (Right inset: Flow chart of related multiphysics for the principle).

$$\nabla \times \mathbf{E}(\mathbf{r}) = -\frac{\partial \mathbf{B}(\mathbf{r})}{\partial t} \quad (2)$$

where $\mathbf{E}(\mathbf{r})$ is the time-varying electric field. Due to a driven voltage, the eddy current is formed within the conductor and in the plane perpendicular to the $\mathbf{B}(\mathbf{r})$. The current density $\mathbf{J}(\mathbf{r})$ in the radiated area is computed through the Ohm's law

$$\mathbf{J}(\mathbf{r}) = \sigma \mathbf{E}(\mathbf{r}) \quad (3)$$

where σ is the electrical conductivity of the material. Then, the power per unit volume is expressed by the differential form of Joule-Lenz Law as follows

$$P_\sigma = \frac{|\mathbf{J}(\mathbf{r})|^2}{\sigma} = \sigma |\mathbf{E}(\mathbf{r})|^2 \quad (4)$$

By integrating P_σ over the heated volume V , the total power can be written as

$$P = \oint_V P_\sigma dv \quad (5)$$

During the pulse time T_p for heating up, the accumulated energy q within the focused region is calculated by

$$q = \int_{T_p} P dt \quad (6)$$

Due to the absorption of the electromagnetic energy within the conductive material, the temperature field profile will change. The relationship between the transient temperature field, T , and absorbed energy, q , can be described through [20]

$$k \nabla^2 T - \rho c \frac{\partial T}{\partial t} = -q \quad (7)$$

where k , ρ , and c are the thermal inductivity, density, and specific heat capacity, respectively. Followed by the local temperature field in a homogeneous and isotropic elastic material, the ultrasonic wave field is created by the thermo-elastic expansion and recovery due to intermittent heating, which is related to the stress and makes particles vibrate inside the conductor. The phenomenon can be formulated by

$$\mu \nabla^2 \mathbf{u} + (\lambda + \mu) \nabla(\nabla \cdot \mathbf{u}) - \alpha(3\lambda + 2\mu) \nabla(T - T_0) = \rho \frac{\partial^2 \mathbf{u}}{\partial t^2} + \gamma \frac{\partial \mathbf{u}}{\partial t} \quad (8)$$

$$\lambda = \frac{v\xi}{(1+v)(1-2v)} \quad (8a)$$

$$\mu = \frac{\xi}{2(1+\nu)} \quad (8b)$$

where \mathbf{u} is the time-dependent displacement vector field, λ and μ are the Lamé constants, calculated by Eqs. (8a) and (8b) respectively, ξ is the elastic modulus, ν is Poisson's ratio, γ is the acoustic damping coefficient, α is the thermal expansion coefficient, and T_0 is the reference temperature. The material parameters of the rail for the numerical modeling are as follows: $k = 48 \text{ W}/(\text{m}\cdot\text{K})$, $c = 450 \text{ J}/(\text{kg}\cdot\text{K})$, $\rho = 7850 \text{ kg}/\text{m}^3$, $\zeta = 206 \text{ GPa}$, $\nu = 0.3$, $\alpha = 1.3 \times 10^{-5} / \text{K}$, and $\gamma = 0$.

Based on the above-mentioned analysis, multiple physical fields are explored and jointly simulated for the proposed rail internal-flaw inspection scheme. The frequency of the ultrasonic wave should be twice of that of the time-varying current through the coil, which is obtained using Eq. (4). Fig. 2 shows the extracted energy density distribution from the finite element method (FEM) simulations based on Eqs. (1)–(8). It is observed that when the distance to the coil becomes larger, the electromagnetic energy density gets smaller. The energy is mainly distributed around the coil, while less inside the rail, which is caused by magnetic field attenuation and low transfer efficiency between the electromagnetic and thermal energies. Inside the rail, the ultrasonic wave field can be generated and picked up by an air-coupled ultrasonic transducer. By analyzing the collected ultrasonic waves, the early detection of rail internal flaws can be realized. In addition, the flowchart of the related multiphysics for the coil-based electromagnetic-induced TA principle is inset in Fig. 2.

III. SYSTEM STRUCTURE ANALYSIS AND DESIGN

To validate the theory of the proposed rail internal-flaw inspection and implement the experiment, a system prototype is designed and analyzed, consisting of the planar transmitting coil and its lumped parameter extraction, impedance matching network, eddy current distribution, IPT equivalent circuit model, and ultrasonic wave propagation inside the rail.

A. Coil Design and Lumped Parameter Extraction

The coil has attracted great attention in recent years as one of the critical components in the IPT systems, including various residential and industrial applications. Compared with a microwave antenna, the coil can work in the high-power and low-frequency mode with a smaller radiator size. In order to better achieve an impedance matching network and quantify the intensity of the magnetic field, the lumped parameters of the coil need to be extracted accurately.

This paper focuses on a planar coil design. Fig. 3(a) shows the structure of a conventional modeled coil with the planar circular spiral winding. The physical parameters such as inner and outer radii and distribution of turns are swept for optimization using the traditional method. Hundreds of simulation iterations will be required, which is time-consuming, especially for a three-dimensional model. To save time budget, the matrix calculation instead of the parametric sweep is utilized, and then the planar coil with the spiral winding is replaced by a lumped-loops model [21], shown in Fig. 3(b). Several loops are distributed with an equal spacing, and each loop consists of 2 winding turns.

As shown in Fig. 3(c), the existence of the ferrite plate

complicates the calculation of the magnetic field. However, by applying the method of mirror images [22]–[24], the original

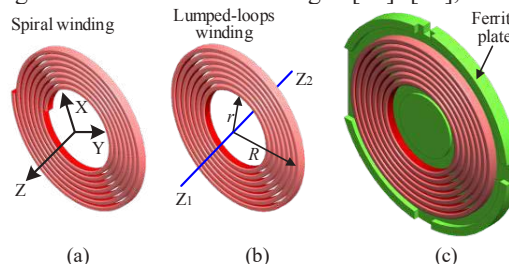


Fig. 3. (a) Structure of planar coil with spiral winding; (b) simplified coil with lumped-loops winding; (c) coil according to (b), using a MnZn ferrite plate.

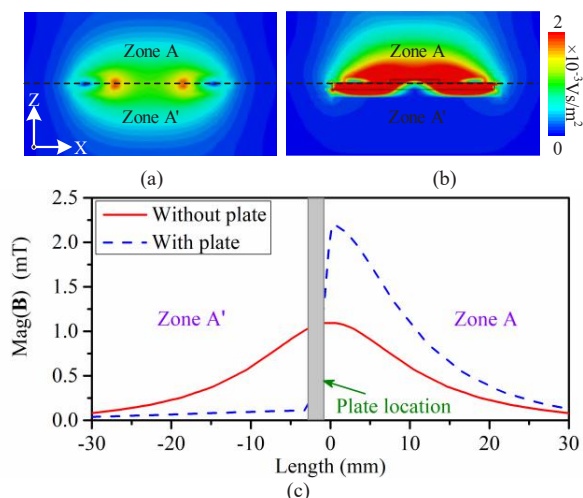


Fig. 4. Magnetic field intensity distribution around simplified coil (a) without and (b) with the ferrite plate; (c) comparison for quantified magnetic fields along the center line of the coil without and with the ferrite plate.

model of the coil with the ferrite plate can be simplified and replaced by an equivalent structure with mirrored turns. The original and mirrored turns are symmetrical about the upper surface of the ferrite plate, conducting the same current. At any point, the magnetic field is the vector addition of both magnetic fields generated by the turns itself and mirrored turns, respectively. Figs. 4(a) and (b) show the magnetic field intensity distributions in the vicinity of the coil without and with the ferrite plates respectively, with the electric current input of the amplitude of 2 A and operating frequency of 2 MHz. For the coil without the ferrite plate, the magnetic fields in Zone A and A' are symmetrical about the plane of the coil (dashed line). When adding the ferrite plate, the magnetic field is enhanced in Zone A, while reduced in Zone A'. The ferrite plate is designed with the radius of 25 mm and thickness of 2 mm and serves following functions: one is to enhance the magnetic field of interest; another is to reduce the leakage magnetic field for the safety consideration. Fig. 4(c) shows the magnitudes of the magnetic fields along the central axis of the coil without and with the ferrite plates. In Zone A, the magnitudes of the magnetic fields generated by the coil with ferrite plate are twice as strong as the ones without ferrite plate, while the values are reduced close to zero in Zone A'.

The planar coil is optimized to reduce the stray magnetic fields by following the description presented in [21], [25]. The Litz wire is selected for the coil design because of the optimal

balance between the efficient power conversion and cost [15]. It is finalized with the outer radius (R) of 21.125 mm and inner

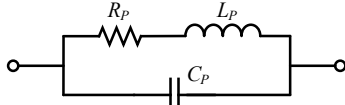


Fig. 5. Lumped parameter model of a coil.

radius (r) of 9.875 mm with 13 turns. The common lumped parameter model of a coil consists of an inductor with inductance L_P , and a resistor with resistance R_P , connected in series, and a distributed parasitic capacitor with capacitance C_P , connected to both terminals in parallel [26], as shown in Fig. 5. The AC resistance R_P is usually divided into two parts: R_{skin} and R_{prox} , caused by skin and proximity effects respectively, as

$$R_P = R_{skin} + R_{prox} \quad (9)$$

Both are generated from the coil itself. For a single strand with the diameter d_s and the current I_s , the skin and proximity effect losses are expressed as P_s^{skin} and P_s^{prox} respectively

$$P_s^{skin} = g^{skin}(f, d_s) \cdot R_{dc} \cdot I_s^2 \quad (10)$$

$$P_s^{prox} = g^{prox}(f, d_s) \cdot R_{dc} \cdot \hat{H}^2 \quad (11)$$

where R_{dc} is the direct-current resistance of the coil. $g^{skin}(f, d_s)$ and $g^{prox}(f, d_s)$ are the skin and proximity effect coefficients respectively, as the functions of the operating frequency f and d_s , and can be expressed with both ber and bei functions derived from Bessel functions of the first kind and order 0/1, as follows [27]–[28]

$$g^{skin}(f, d_s) = \frac{\beta}{2} \cdot \frac{ber(\beta)bei'(\beta) - bei(\beta)ber'(\beta)}{ber'^2(\beta) + bei'^2(\beta)} \quad (12)$$

$$g^{prox}(f, d_s) = \frac{-2\pi\beta}{\sigma} \cdot \frac{ber_2(\beta)ber'(\beta) + bei_2(\beta)ber'(\beta)}{ber^2(\beta) + bei^2(\beta)} \quad (13)$$

herein

$$\beta = \frac{d_s}{\delta\sqrt{2}} \quad (14)$$

and skin depth

$$\delta = \sqrt{\frac{1}{\pi f \mu_0 \mu_r \sigma}} \quad (15)$$

where μ_r and σ are the relative permeability and copper conductivity, respectively. Given the Litz wire is with n_s strands, as well as the I_s and P_s^{prox} in each strand are the same, R_P can be written as

$$R_P = \frac{2 \cdot P_{loss}(f)}{(n_s \cdot I_s)^2} = \frac{2 \cdot n_s \cdot (P_s^{skin} + P_s^{prox})}{(n_s \cdot I_s)^2} \quad (16)$$

Substituting Eqs. (10) and (11) into (16) gives

$$R_P = \frac{2 \cdot n_s \cdot (g^{skin}(f, d_s) \cdot I_s^2 + g^{prox}(f, d_s) \cdot \langle \hat{H}_{\perp}^2 \rangle_b)}{(n_s \cdot I_s)^2} \cdot R_{dc} \quad (17)$$

where $\langle \hat{H}_{\perp}^2 \rangle_b$ is the spatial average of the effective transverse magnetic field, which is extracted from FEM simulation, or analytically calculated by

$$\langle \hat{H}_{\perp}^2 \rangle_b = \frac{I_b^2}{8\pi^2 r_b^2} \quad (18)$$

The copper wire adopted has the radius $r_b = 0.575$ mm, $n_s = 110$, $d_s = 0.08$ mm, and $I_b = n_s \times I_s$. By combining Eqs. (17) and (18), R_P is calculated through MATLAB and plotted in Fig. 6(a), wherein the measured R_{dc} is 0.28 Ω . Also, the inductance of the coil is calculated using FEM simulation and the value is

kept almost invariant to the frequency, shown in Fig. 6(b). However, when removing the ferrite plate, the inductance will

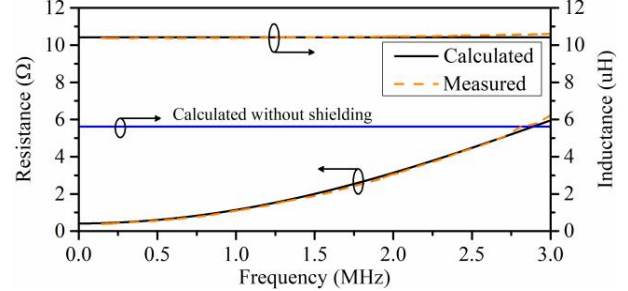


Fig. 6. Measured and calculated results of extracted parameters for the coil: Resistance and Inductance.

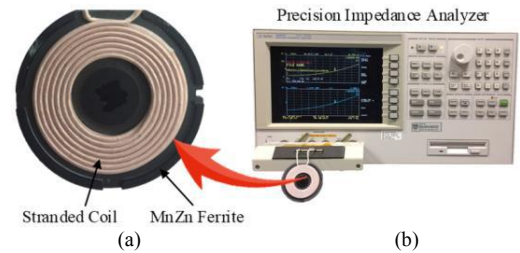


Fig. 7. (a) Fabricated prototype of the planar stranded coil, and (b) test setup.

be reduced by half due to the absence of the magnetic wall.

The fabricated coil is measured by an Impedance Analyzer (Agilent 4294A), as shown in Fig. 7. The measured resistance and inductance data are shown in Figs. 6(a) and (b) respectively, both of which are consistent with the calculated results for the coil with the ferrite plate. It is seen that the resistance and inductance at 2.03 MHz are 2.84 Ω and 10.557 μH , respectively, where the measured quality factor is about 46.1. Then, the C_P in the coil can be calculated by

$$C_P = \frac{1}{(2\pi f_s)^2 \cdot L_P} \quad (19)$$

where f_s and L_P are the self-resonant frequency and corresponding inductance, respectively. The measured f_s is at 11.5 MHz. Applying Eq. (19), the C_P is calculated to be 18.4 pF.

B. Impedance Matching Network

To make most power effectively flow into the planar coil from an RF power amplifier, the output impedance of the amplifier should be equal to the input impedance of the coil. However, the coil has a high input reflection coefficient due to high inductance and low resistance. Thus, an impedance matching network is required between the amplifier and coil. The L-type matching network is employed and designed to reduce the reflection and efficiently deliver the power to the rail due to the high-quality factor and easy implementation [29].

All capacitor components are selected to fulfill complex conjugate matching for the inductive input impedance of the coil, shown in Fig. 8(a). The total series capacitance is 691 pF, including one 470 pF, four 47 pF and one 33 pF capacitors connected in parallel, and the parallel capacitance is 4 nF, consisting of four 1 nF capacitors connected in parallel. The corresponding schematic circuit is depicted in Fig. 8(b). Due to the parasitic resistances of the capacitors, long pins, and welded joints, an equivalent extra resistance R_{MC} is included in the fabricated prototype, which is measured by the Network

Analyzer. Fig. 8(c) shows the measured and simulated results, which coincide with each other. As shown, the measured

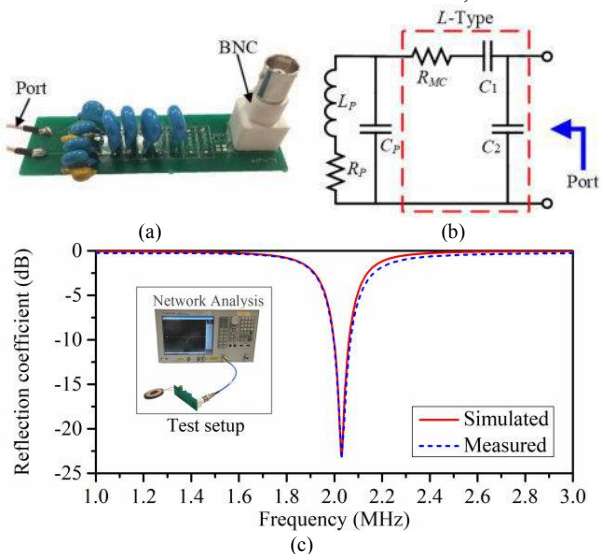


Fig. 8. L-type impedance matching network. (a) Fabricated prototype, (b) schematic circuit, and (c) measured and simulated results (Inset: Test setup).

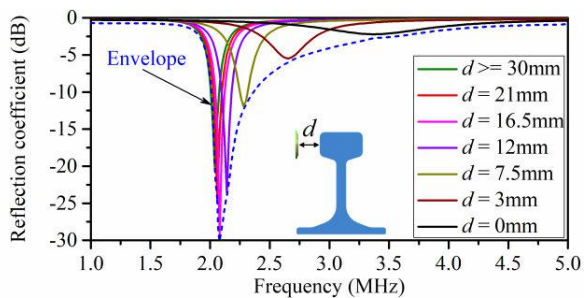


Fig. 9. Measured reflection coefficients of matching network under different lift-off distances between the coil and rail.

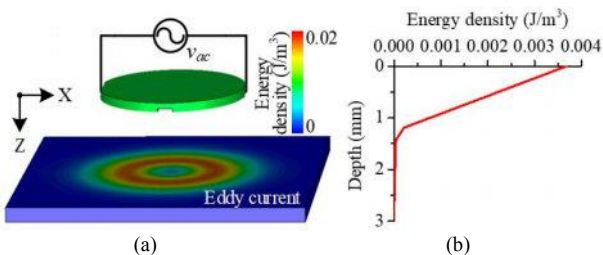


Fig. 10. (a) Eddy current, and (b) relationship of depth and energy density.

reflection coefficient is -23.62 dB at the center frequency of 2.03 MHz, with the bandwidth from 1.99 to 2.08 MHz under the -10 dB level, and the input impedance is 54.48 Ω at 2.07 MHz. Fig. 9 is plotted for the magnitude change of the reflection coefficient of impedance matching network with varying lift-off distance d between the coil and rail. The reflection coefficient is a function of the frequency f and d , and can be written as $R(f, d)$. As the d decreases, the center frequency of $R(f, d)$ moves toward the high range due to the influence of mutual coupling. The magnitude can be fitted as

$$|R(f, d)| = \sum_{i=1}^5 a_i \cdot \exp\left(-\left(\frac{f-b_i}{c_i}\right)^2\right) \quad (20)$$

where a_i , b_i and c_i are related to d and expressed respectively as

$$a_i(d) = \sum_{j=1}^6 a_{ij} \cdot d^{6-j} \quad (20a)$$

$$b_i(d) = \sum_{j=1}^6 b_{ij} \cdot d^{6-j} \quad (20b)$$

$$c_i(d) = \sum_{j=1}^6 c_{ij} \cdot d^{6-j} \quad (20c)$$

where a_{ij} , b_{ij} and c_{ij} are respectively the entries in (i, j) of the corresponding matrixes **A**, **B** and **C**,

$$\mathbf{A} = \begin{bmatrix} 0 & -0.014 & 0.2693 & -2.103 & 4.629 & -0.197 \\ 0 & 0.0193 & -0.347 & 2.432 & -5.627 & -1.233 \\ 0 & -0.001 & 0.0214 & -0.125 & 0.069 & -0.95 \\ 0.0397 & -2.267 & 46.43 & -402.8 & 1240 & -2.406 \\ 0 & -0.001 & 0.0198 & -0.159 & 0.5237 & -0.821 \end{bmatrix}$$

$$\mathbf{B} = \begin{bmatrix} 79.28 & -3922 & 62630 & -307500 & -358400 & 4090000 \\ 36.96 & -1553 & 15640 & 72490 & -1263000 & 2830000 \\ 36.29 & -1491 & 13710 & 98480 & -1405000 & 3070000 \\ -32.39 & 1943 & -43360 & 441600 & -1994000 & 3030000 \\ -37.2 & 2232 & -49800 & 507200 & -2291000 & 3480000 \\ -79.73 & 4792 & -107100 & 1094000 & -4950000 & 7530000 \end{bmatrix}$$

$$\mathbf{C} = \begin{bmatrix} -2.01 & 153.2 & -4329 & 54940 & -291500 & 485000 \\ 14.46 & -677.9 & 9921 & -39660 & -65170 & 336000 \\ -6.296 & 377.7 & -8428 & 85840 & -387700 & 589000 \\ -9.898 & 593.9 & -13250 & 135000 & -609500 & 926000 \end{bmatrix}$$

Eq. (20) can reflect the relationship between the coil and rail. For different d , there always exists a minimum value in Eq. (20) and all minimum values forms the envelope, shown in Fig. 9. The envelope is fitted as

$$ENV = \sum_{j=1}^5 m_{1j} \cdot \exp\left(-\left(\frac{f-m_{2j}}{m_{3j}}\right)^2\right) \quad (21)$$

where m_{1j} , m_{2j} and m_{3j} are respectively the corresponding entries in $(1, j)$, $(2, j)$ and $(3, j)$ of the matrix **M**,

$$\mathbf{M} = \begin{bmatrix} -1.651 & -10.23 & -21.73 & -4.542 & -1.936 \\ -2.928 & -0.1183 & -0.247 & 0.3236 & 0.9829 \\ 1.669 & 0.2002 & 0.06418 & 0.4931 & 1.406 \end{bmatrix}$$

Each point on the envelope represents an ideal working condition of impedance matching network at given frequency, which has a maximum transmission efficiency.

C. Eddy Current Distribution

When the railhead is illuminated by the magnetic field generated from the coil, the eddy currents will be induced within the conductor based on Faraday's law of induction. The Lenz's law shows that the induced current loops generate a magnetic field that opposes changes of the magnetic field which created it, where the magnetizing field \mathbf{B}_S is evaluated by

$$\nabla \times \mathbf{B}_S = \mu_0 \mathbf{J}(\mathbf{r}) \quad (22)$$

Due to the resistive losses from the eddy currents, one part of the electrical energy is converted into the thermal energy, consumed in the conductor; another part is stored in the induced electromagnetic field, further reacting against the source of the magnetic field. The induced eddy current and the current in the coil are in the opposite directions, and the former has a weaker current density, which is observed from the simulation result. Due to the skin effect, the thermal energy mainly concentrates on the superficial layer of the railhead. Also, the relationship between energy density and depth is depicted in Fig. 10. As the depth increases, the energy density becomes smaller. At the depth of 1.5 mm, the energy density is close to zero. The thermal energy loss in the rail is evaluated by Eq. (6).

D. Equivalent Circuit Model of the Coil-Rail Coupling

According to the relationship between the eddy currents in the rail and the currents through the coil, the interaction from

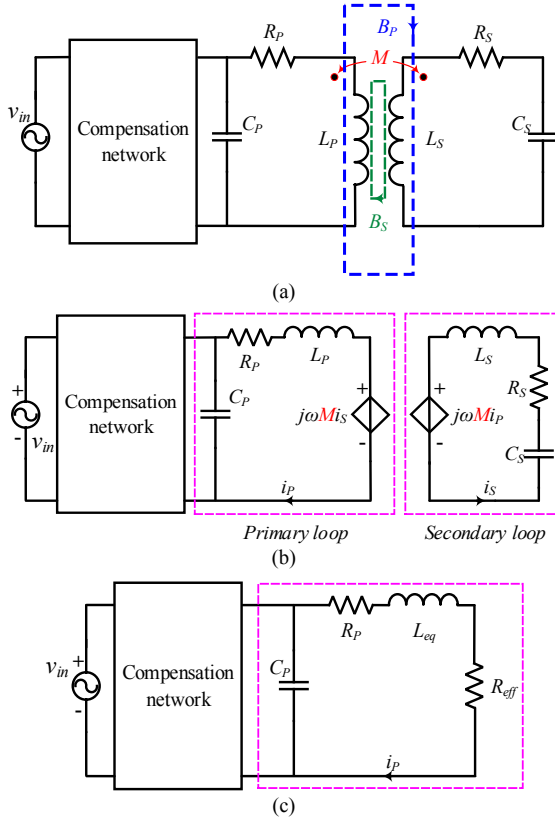


Fig. 11. IPT topology. (a) Transformer model of the excitation coil of eddy current and rail specimen under test, (b) equivalent circuit model, and (c) simplified equivalent circuit model.

the electrical energy to thermal energy can be equivalently modeled as an IPT system, consisting of two inductors and their corresponding inherent circuits, as shown in Fig. 11. For the proposed rail internal-flaw inspection scheme shown in Fig. 1, the power is dissipated in the rail, windings, and ferrite plate. The ferrite plate is utilized to minimize power losses in the frequency range of interest and enhance the dissipation in the rail because it is the magnetic wall which behaves like a mirror [30]. Ignoring the loss in the ferrite plate, this paper mainly analyzes the power transferred to the rail and the winding losses. Transformer model of the planar coil and the eddy current loop is shown in Fig. 11(a), denoted as the primary and secondary loops, respectively. The secondary circuit modeling the rail effect consists of an inductance, L_S , capacitance, C_S , and resistance, R_S , connected in series. Inductances L_P in the primary loop, L_S in the secondary loop, and mutual inductance M are basic components of the transformer model. In addition, C_P and C_S are their corresponding parasitic capacitances. R_P and R_S are the equivalent resistances of the primary and secondary loops, respectively. The matching network is implemented to enhance power transfer from AC source v_{in} to R_S . The AC source is usually a pulse current with a repetition frequency, or low-frequency modulated pulse with the high-frequency carrier frequency ω .

In the subsequent analysis, a frequency-domain equivalent

circuit is adopted and only R_P , R_S , L_P , L_S , C_P , and C_S are considered here for simplicity. Fig. 11(b) displays an equivalent circuit of Fig. 11(a) for the analysis of steady-state condition. The current-dependent source $\omega M i_S$ in Fig. 11(b) can be replaced by an equivalent impedance Z_r which is calculated by dividing $\omega M i_S$ with i_P . In this way, the primary loop is decoupled from the secondary loop and Z_r is derived as

$$Z_r = \frac{\omega^2 M^2}{Z_S} \quad (23)$$

where Z_S is the impedance of the secondary loop, given by

$$Z_S = j\omega L_S + \frac{1}{j\omega C_S} + R_S \quad (24)$$

Power transfer efficiency is defined as the ratio of the power transferred to the rail and power supplied by the compensation network. Moreover, another expression can be obtained by solely considering active power and thus the efficiency η_P in the primary loop is expressed as

$$\eta_P = \frac{\text{Re}(Z_r)}{R_P + \text{Re}(Z_r)} \quad (25)$$

Herein,

$$\text{Re}(Z_r) = \frac{\omega^2 M^2 R_S}{R_S^2 + X_S^2} = \frac{\omega^2 k^2 L_P L_S R_S}{R_S^2 + X_S^2} \quad (26)$$

where

$$X_S = \omega L_S - \frac{1}{\omega C_S} \quad (27)$$

and the coupling coefficient is given by

$$k = \frac{M}{\sqrt{L_P L_S}} \quad (28)$$

Considering all electrical energy is converted into the heat, the efficiency η_S in the secondary loop is assumed to be 1. Thereby, the IPT efficiency η_T is defined as follows

$$\eta_T = \eta_P \eta_S \quad (29)$$

The R_S , L_S , and C_S are difficult to be tested accurately, since they are related to operating frequency, transmitting coil size, input current, the distance between the coil and rail, etc. The IPT equivalent circuit model can be further simplified and shown in Fig. 11(c). Herein L_{eq} is the total inductance taking into account the effect of the rail, and R_{eff} is the increment of equivalent resistance, respectively calculated by

$$L_{eq} = L_P - \frac{\text{Im}(Z_r)}{j\omega} \quad (30)$$

$$R_{eff} = \text{Re}(Z_r) \quad (31)$$

Both L_{eq} and R_{eff} can be measured and drawn in Fig. 12. When the reflection coefficient of matching network is located at the envelope curve as shown Fig. 9, the corresponding input impedance is measured, including the real and imaginary parts drawn in Fig. 13. The matching network and simplified equivalent circuit model are built in Agilent ADS, where Z_{in} and Z_T represent the corresponding input impedances, shown in Fig. 14. The measured Z_{in} is imported to obtain the L_{eq} and R_{eff} , where the simulated results are consistent with the measured data, shown in Fig. 12. When measured L_{eq} and R_{eff} are imported, the real and imaginary parts of Z_{in} are thus simulated and shown to be in good agreement with the measured data, which are shown in Fig. 13.

As shown in Fig. 14, Z_{in} and Z_T are derived as

$$Z_{in} = \frac{1}{j\omega C_2} // \left(\frac{1}{j\omega C_1} + R_{MC} + Z_T \right) \quad (32)$$

$$Z_T = \frac{1}{j\omega C_P} // (R_P + L_{eq} + R_{eff}) \quad (33)$$

Besides, Z_{in} can also be expressed by

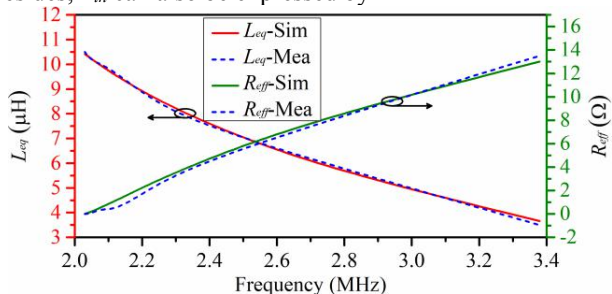


Fig. 12. Measured and simulated data for L_{eq} and R_{eff} .

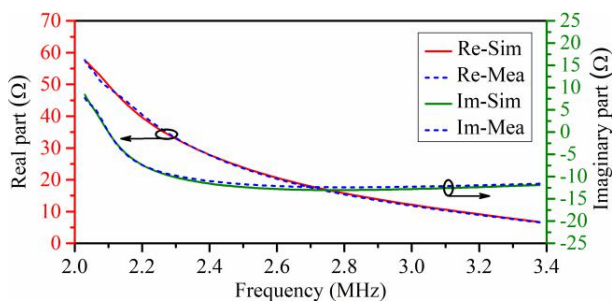


Fig. 13. Measured and simulated data of real and imaginary parts.

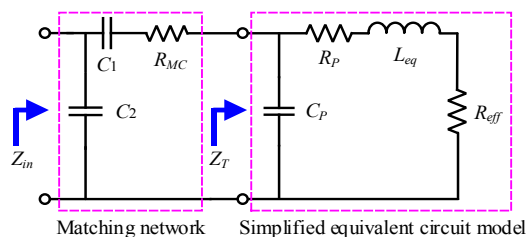


Fig. 14. Combination of matching network and simplified equivalent circuit model.

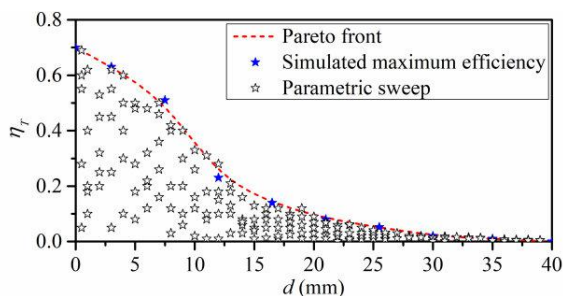


Fig. 15. Pareto front of the η_T versus d .

$$Z_{in} = 50 \times \frac{1+R(f,d)}{1-R(f,d)} \quad (34)$$

Combing Eqs. (32) - (33), R_{eff} can be extracted as a function of f and d . The IPT efficiency η_T can be rewritten as

$$\eta_T = \frac{R_{eff}}{R_P + R_{eff}} \quad (35)$$

Since η_T is closely related to the f and d , the synergetic optimization becomes important. Accordingly, the Pareto front is introduced and implemented. The front is plotted on a two-

dimensional Cartesian coordinate system. The horizontal axis and vertical axis represent the distance and IPT efficiency, respectively, as shown in Fig. 15. Each marker represents the η_T under the condition of given f and d values. The Pareto front is then plotted on the upper right of all the markers, indicating

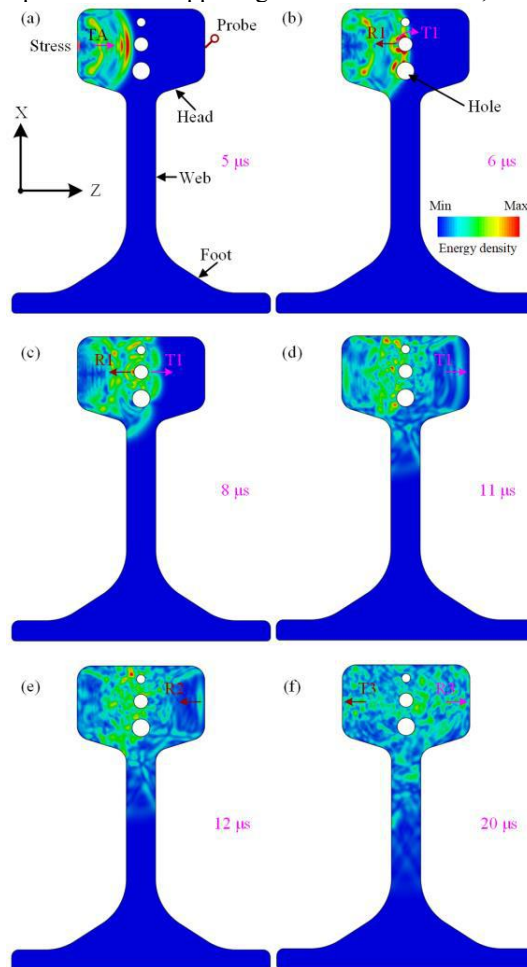


Fig. 16. Ultrasonic wave propagation in railhead with holes during (a) 5 μ s, (b) 6 μ s, (c) 8 μ s, (d) 11 μ s, (e) 12 μ s, and (f) 20 μ s.

by the dashed line. When the working condition for the radiating coil meets the Eq. (21), the efficiencies are highlighted and distributed close to the Pareto front. When d is invariant, the coil can resonate at a specific frequency and radiate the energy with maximum efficiency.

E. Ultrasonic Wave Propagation

To investigate the ultrasonic wave propagating through the conductive material and its interactions with the flaws in the rail, the simulations are performed. When the high-power energy is loaded on the specific area of the rail, the area is rapidly heated and deformed. Alternating heating leads to the mechanical vibration and creates the ultrasonic wave. The rail with and without three holes are respectively modeled in Abaqus, and a modulated excitation is added in Load module, where the carrier is the sinusoidal signal with the frequency of 2.1 MHz and current magnitude of 1 A, and modulating signal is the square wave with the frequency of 100 Hz and width of 1 μ s. The stress/displacement, the electric/magnetic vector

potential and the temperature fields are simultaneously solved with the coupled thermal-electromagnetic-structural analysis. Thereby the stress is produced inside the railhead, and the ultrasonic wave propagation can be observed over time. Several screenshots at different time instances, i.e., 5, 6, 8, 11, 12, and 20 μs , are illustrated in Fig. 16.

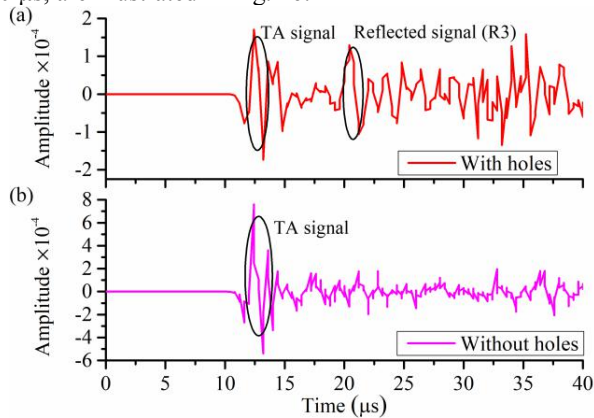


Fig. 17. Collected signals at the receiver probe (a) with holes, and (b) without holes.

On the opposite side of the railhead, a probe is placed for picking up the ultrasonic wave signals. Both of the rails with and without holes are analyzed, and the corresponding collected signals are displayed in Fig. 17. When the propagating ultrasonic waves (TA) meet the holes, part (R1) of them is reflected; the remaining part (T1) bypasses the holes and continues to spread until it meets the interface between the rail and air (At this point of time, the first peak is recorded with the Probe, denoted as TA signal). On the interface, the ultrasonic waves are partly reflected to move forward. When these (R2) meet the holes for the second time, only part of them (R3) is reflected again and spreads as well as arrives at the probe (At this point of time, the second peak value is recorded, named Reflected signal). The first and second peak values can be observed in Fig. 17(a), however, the second doesn't exist in the rail without holes, shown in Fig. 17(b). Over time, the reflected waves from different directions are superimposed and form the quasi-static response. By analyzing the received signals, the flaws inside the rail can be identified and thus detected.

IV. MEASUREMENT, RESULTS AND DISCUSSION

A. Measurement Setup

The measurement instruments and specimen used to implement the experiment are shown in Fig. 18. The RF function generator (Tektronix AFG3022) provides two kinds of signals. One is the sinusoidal wave with an operating frequency (e.g., 2 MHz) and amplitude of 10 Vpp, which is feed into the power amplifier (Tomco RF Pulse Amplifier, up to 300 W peak power), and then is delivered to the planar coil through the impedance matching network. Another is the trigger pulse with the frequency of 100 Hz and amplitude of 10 Vpp, which is connected to both power Amplifier and digital phosphor oscilloscope (Tektronix TDS5052B) by a two-way splitting divider. The oscilloscope is also connected with the ultrasonic transducer (A551S-SM, Olympus). During a wide gating period, the reflected signals are difficult to be picked up since

they are easy to overlap with the excitation signal due to rapid ultrasound inside the rail. Thus, the pulse width of 1 μs for the RF power amplifier is selected. Different modules are connected by the RF coaxial cable assembling BNC (50 Ω , Pomona Electronics Model 2249).

Then, the TA signal generated by absorbed electromagnetic energy in the rail is picked up by the ultrasonic transducer with

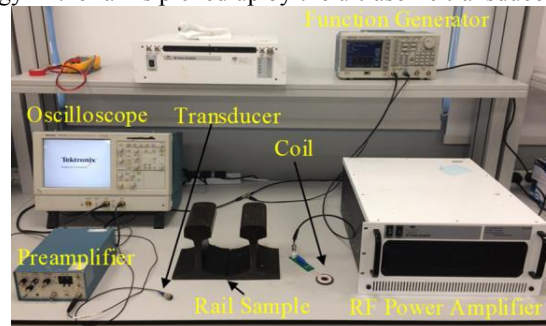


Fig. 18. Photograph of the measurement setup and environment.

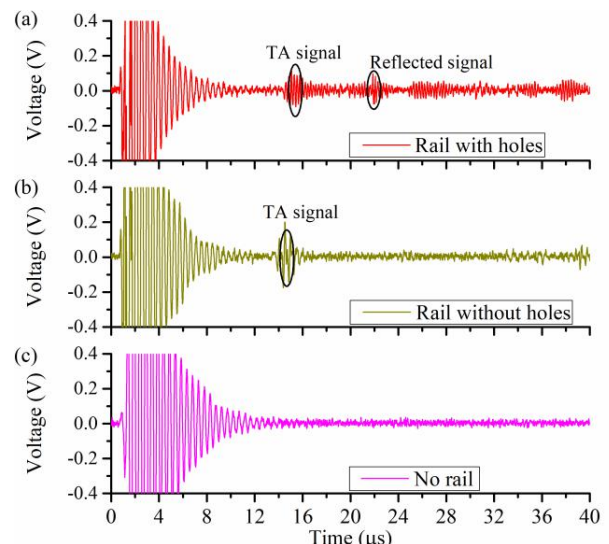


Fig. 19. Measured TA signals at 2.0765 MHz for different cases under (a) I: rail with holes, (b) II: rail without holes, and (c) III: no rail.

a center frequency of 5 MHz and relative bandwidth of about 50%, followed by the preamplifier with a gain of 59 dB (Model 5077PR, 35 MHz Manually Controlled Ultrasonic Square Wave Pulser-receiver, Olympus). The sinusoidal wave, the trigger pulse, and the TA signal are simultaneously recorded with the oscilloscope at the rate of 2.5 G samples/s.

B. TA Signal and Internal-Flaw Detection

The experiment is implemented to verify the feasibility of the proposed system for the rail internal-flaw inspection. It employs the coil as the excitation source and shows potential to increase the lift-off distance between the transmitting circuit and rail. Three holes are drilled in the railhead of the specimen (UCI 60, the width of the head is 72 mm, the height is 172 mm and the length is 150 mm) with the diameters of 5 mm, 8 mm, and 10 mm as the cracks and are perpendicular to the cross-section of the rail. The coil and transducer are respectively placed on both sides of the railhead and their axes are coincident. The induced TA signal propagates through the railhead and will be reflected

when meeting the cracks and interface between the rail and air. The internal holes can scatter and attenuate the signal, thus changing its propagation path and amplitude.

The TA signal will arrive at the receiver transducer in the time t_d , calculated by

$$t_d = \frac{w}{v_a} \quad (36)$$

where w is the railhead width, and v_a is the sound speed inside

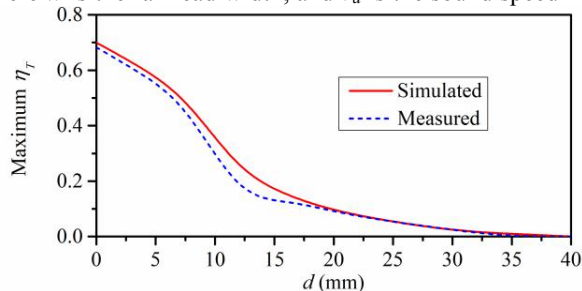


Fig. 20. Maximum IPT efficiency from the planar coil to rail.

the rail. Due to $d = 72$ mm and $v_a = 5150$ m/s, t_d is calculated to be about $14 \mu\text{s}$, which is consistent with the measured results, as shown in Fig. 19. In the figure, different measured TA signals are also illustrated for different cases under (I) rail with holes, (II) rail without holes, and (III) no rail between the coil and transducer at 2.0765 MHz, respectively. For the rail with/without holes, the lift-off distance between the coil and rail is about 16.5 mm, where they satisfy the smallest value of the envelope curve in Fig. 9 and can resonate at 2.0765 MHz. As shown in Fig. 19, the TA signals are clearly observed in the cases (I) and (II), and the amplitude of the TA signal in case (I) is smaller than the one in case (II) due to energy scattering by the holes. When the TA signal arrives at the receiver interface and then is partially reflected, the first reflected signal propagates and is reflected again by the holes. The second reflected signal is also observed with a smaller amplitude due to multiple reflections, shown in Fig. 19(a), which is consistent with the simulation result in Fig. 17(a). When the lift-off distance between the coil and rail reduces to 3 mm, the radiating coil resonates at 2.665 MHz. The same three cases (I), (II), and (III) are investigated and the corresponding measured results are analyzed. The amplitudes of TA and reflected signals are smaller than the ones in Fig. 19, since the compensation network is shifted to the non-matching state with the change of frequency and the available power from the coil is reduced. Through the comparison, the lift-off distance can be enlarged by adding the impedance matching network.

C. IPT Efficiency

The IPT efficiency is related to the frequency and distance between the coil and rail. Referring to Eq. (21), the maximum IPT efficiencies are measured at different distances, which coincide with the simulated ones, as drawn in Fig. 20. As shown, when the d is 16.5 mm and 3 mm, the measured IPT efficiencies are 12.93% and 60.82%, respectively. However, the former case gets better matching and reduces the loss in the impedance matching network. Thereby, the more effective power is obtained in the rail.

D. Magnetic Field around the Coil

Fig. 21(a) shows the side view of the planar coil and rail as well as the measurement points for the magnetic fields along the Y and Z axes. For each position, the near-field probe Langer EMV LF-R 50 is utilized to measure magnetic fields $B_x(t)$, $B_y(t)$ and $B_z(t)$ in the X/Y/Z directions. The quantified magnetic fields are calculated using [21]

$$B = \sqrt{B_x^2 + B_y^2 + B_z^2} \quad (37)$$

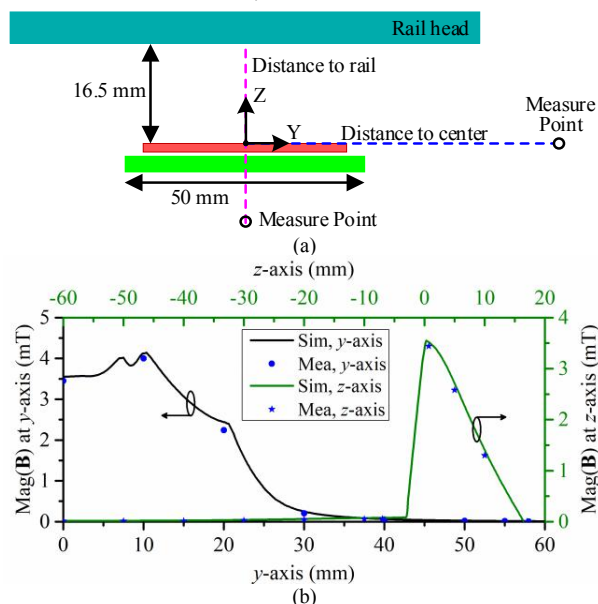


Fig. 21. (a) Side view of the coil and rail as well as points for field measurement along the Y/Z axis, and (b) quantified magnetic fields along y/z-axis, which are simulated and measured.

With a 16.5 mm gap between the coil and railhead, the magnetic fields along the y/z-axis are simulated and measured for the radiating coil, as shown in Fig. 21(b). The origin of the coordinate system is placed at the center point of the coil, and the points of field measurement are located along the dashed line in Fig. 21(a). For Z direction, the distance to the railhead varies from -60 mm to 20 mm, while for Y direction, the distance to the center of the coil ranges from 0 to 60 mm. The difference between measurement and simulation is less than 11.9%. At the center point of the eddy current loop, the measured magnetic field is about $72 \mu\text{T}$.

V. CONCLUSION

The coil-based electromagnetic-induced TA fundamental has been investigated to inspect the internal flaws in the rail, which leads to a promising non-contact and low-cost methodology for examining cracks inside the conductive material. The TA signal has been generated by the thermal expansion through a time-varying magnetic field excited by a planar coil. By adding a ferrite plate, it reduces exposure to electromagnetic fields in the non-working region and doubles the intensity of the magnetic field. The lumped parameters of resistance, inductance, and capacitance of the coil are extracted through the numerical analysis and experiment. Then, the impedance matching network is designed to efficiently transmit power from the RF power amplifier to the coil. The equivalent circuit model is

developed and further simplified to quantitatively characterize the IPT between the coil and rail. Furthermore, the IPT efficiency is simulated and tested with the increase of the lift-off distance. Finally, the experimental setup has been built and the clear TA signal changes due to inside the rail with/without flaws have been observed. Future work will improve the detection accuracy for small crack size and further optimize the circuits for optimal IPT efficiency.

ACKNOWLEDGMENT

This research work was conducted in the SMRT-NTU Smart Urban Rail Corporate Laboratory with funding support from the National Research Foundation (NRF), SMRT and Nanyang Technological University; under the Corp Lab@University Scheme.

REFERENCES

- [1] T. Oe, Y. Nawa, N. Tsuda, and J. Yamada, "Nondestructive internal defect detection using photoacoustic and self-coupling effect," *Electr. Commun. Jpn.*, vol. 93, no. 7, pp. 17-22, 2010.
- [2] T. Tanaka and Y. Izawa, "Nondestructive detection of small internal defect in carbon steel by laser ultrasonics," *Jpn. J. Appl. Phys.*, vol. 40, no. 1, pp. 1477-1481, 2001.
- [3] R. Ribichini, F. Cegla, P. B. Nagy, and P. Cawley, "Study and comparison of different EMAT configurations for SH wave inspection," *IEEE Trans. Ultrason. Ferroelectr. Freq. Control*, vol. 58, no. 12, pp. 2571-2581, Dec. 2011.
- [4] J. Isla and F. Cegla, "EMAT phased array probe for detecting surface cracks," in *Proc. IEEE ISAF/IWATMD/PFM*, Atlanta, GA, USA, Aug. 2017, pp. 1-4.
- [5] A. G. Bell, "Upon the production and reproduction of sound by light," *J. Soc. Telegraph Eng.*, vol. 9, no. 34, pp. 404-426, 1880.
- [6] L. V. Wang, *Photoacoustic Imaging and Spectroscopy*, Boca Raton, FL, USA: CRC Press, 2009.
- [7] Z. Deng and C. Li, "Noninvasively measuring oxygen saturation of human finger-joint vessels by multi-transducer functional photoacoustic tomography," *J. Biomed. Opt.*, vol. 21, no. 6, pp. 061009-1-061009-5, 2016.
- [8] K. Sivasubramanian and M. Pramanik, "High frame rate photoacoustic imaging at 7000 frames per second using clinical ultrasound system," *Biomed. Opt. Exp.*, vol. 7, no. 2, pp. 312-323, 2016.
- [9] Laser-air, hybrid, ultrasonic testing of railroad tracks, by S. Kenderian, B. B. Djordjevic, R. E. Green, Jr., D. Cerniglia. (2005, Sep. 20). Patent US6945114B2
- [10] S. Boonsang and R. J. Dewhurst, "Signal enhancement in Rayleigh wave interactions using a laser-ultrasound/EMAT imaging system," *Ultrasonics*, vol. 43, no. 7, pp. 512-523, 2005.
- [11] M. S. Aliroteh and A. Arbabian, "Microwave-induced thermoacoustic imaging of subcutaneous vasculature with near-field RF excitation," *IEEE Trans. Micro. Theory Tech.*, vol. 66, no. 1, pp. 577-588, Jan. 2018.
- [12] X. Feng, F. Gao, and Y. Zheng, "Magnetically mediated thermoacoustic imaging toward deeper penetration," *Appl. Phys. Lett.*, vol. 103, no. 8, pp. 083704-1-083704-4, 2013.
- [13] S. Kellnberger, M. Omar, G. Sergiadis, and V. Ntziachristos, "Second harmonic acoustic responses induced in matter by quasi continuous radiofrequency fields," *Appl. Phys. Lett.*, vol. 103, no. 15, pp. 153706-1-153706-4, 2013.
- [14] D. M. Pozar, *Microwave Engineering*, 4th ed, Hoboken, NJ, USA: Wiley, 2012.
- [15] I. Lope, J. Acero, and C. Carretero, "Analysis and optimization of the efficiency of induction heating applications with litz-wire planar and solenoidal coils," *IEEE Trans. Power Electron.*, vol. 31, no. 7, pp. 5089-5101, Jul. 2016.
- [16] W. Zhang, J. C. White, R. K. Malhan, and C. C. Mi, "Loosely coupled transformer coil design to minimize EMF radiation in concerned areas," *IEEE Trans. Veh. Technol.*, vol. 65, no. 6, pp. 4779-4789, Jun. 2016.
- [17] D. R. Agrawal, Y. Tanabe, D. Weng, A. Ma, S. Hsu, S. Y. Liao, Z. Zhen, Z. Y. Zhu, C. Sun, Z. Dong, F. Yang, H. F. Tse, A. S. Y. Poon, and J. S. Ho, "Conformal phased surfaces for wireless powering of bioelectronics microdevices," *Nat. Biomed. Eng.*, vol. 1, no. 0043, pp. 1-9, Mar. 2017.
- [18] R. Nopper, R. Has, and L. Reindl, "A wireless sensor readout system-circuit concept, simulation, and accuracy," *IEEE Trans. Instrum. Meas.*, vol. 60, no. 8, pp. 2976-2983, Mar. 2011.
- [19] S. H. Yeung, R. Pradhan, X. Feng, and Y. Zheng, "Focused magnetic resonance coupling coils for electromagnetic therapy applications," *IEEE Trans. Biomed. Eng.*, vol. 62, no. 11, pp. 26.2-2610, Nov. 2015.
- [20] C. Pei, K. Demach, H. Zhu, T. Fukuchi, K. Koyama, M. Uesaka, "Inspection of cracks using laser-induced ultrasound with shadow method: modeling and validation," *Opt. Laser Technol.*, vol. 44, pp. 860-865, 2012.
- [21] M. Lu and K. D. T. Ngo, "A fast method to optimize efficiency and stray magnetic field for inductive-power-transfer coils using lumped-loops model," *IEEE Trans. Power Electron.*, vol. 33, no. 4, pp. 3065-3075, May 2017.
- [22] A. V. den Bossche and V. C. Valchev, *Inductors and Transformers for Power Electronics*. Boca Raton, FL: CRC Press/Taylor Francis Group, 2005.
- [23] W. A. Roshen and D. E. Turcotte, "Planar inductors on magnetic substrates," *IEEE Trans. Magn.*, vol. 24, no. 6, pp. 3213-3216, Nov. 1988.
- [24] J. Muhlethaler, M. Schweizer, R. Blattmann, J. W. Kolar and A. Echelebe, "Optimal design of LCL Harmonic Filters for three-phase PEC rectifiers," *IEEE Trans. Power Electron.*, vol. 28, no. 7, pp. 3114-3125, Jul. 2013.
- [25] M. Lu and K. D. T. Ngo, "Attenuation of stray magnetic field in inductive power transfer by controlling phases of windings' currents," *IEEE Trans. Magn.*, vol. 53, no. 9, pp. 8700408-1-8700408-8, Jun. 2017.
- [26] A. Massarini and M. K. Kazimierczuk, "Self-capacitance of inductors," *IEEE Trans. Power Electron.*, vol. 12, no. 4, pp. 671-676, Jul. 1997.
- [27] J. A. Ferreira, "Improved analytical modeling of conductive losses in magnetic components," *IEEE Trans. Power Electron.*, vol. 9, no. 1, pp. 127-131, Jan. 1994.
- [28] R. L. Stoll, *The Analysis of Eddy Currents*, Oxford: Clarendon Press, 1974.
- [29] C. L. Yang, C. K. Chang, S. Y. Lee, S. J. Chang, and L. Y. Chiou, "Efficient four-coil wireless power transfer for deep brain stimulation," *IEEE Trans. Micro. Theory Tech.*, vol. 65, no. 7, pp. 2496-2507, Apr. 2017.
- [30] J. Acero, C. Carretero, R. Alonso, and J. M. Burdío, "Quantitative evaluation of induction efficiency in domestic induction heating applications," *IEEE Trans. Magn.*, vol. 49, no. 4, pp. 1382-1389, Apr. 2013.

Wensong Wang received the Ph.D. degree from the Nanjing University of Aeronautics and Astronautics, Nanjing, China, in 2016.

From 2013 to 2015, he was a Visiting Scholar with the University of South Carolina, Columbia, USA. In 2017, he joined Nanyang Technological University, Singapore, as a Research Fellow.

His research interests include RF/microwave components and systems, inter/intra-chip wireless interconnect, power wireless transfer, signal integrity, and rail non-destructive real-time monitoring.



Zilian Qu received the Ph.D. degree in Mechanical Engineering from Tsinghua University, Beijing, China, in 2014.

From 2014 to 2016, he was a Postdoctoral Research Associate with the Tsinghua University, China. From 2016 to 2017, he was a Research Fellow with the SMRT-NTU Smart Urban Rail Corporate Laboratory in Nanyang Technological University, Singapore. He is currently an Assistant Professor with the Beijing Information Technology College in China. His current research interests include non-destructive testing and evaluation, design of electromagnetic sensor and manufacturing technology of integrated circuit. He is a senior member of Chinese Mechanical Engineering Society (CMES).





Zesheng Zheng was born in Fujian Province, China. He received the B.Eng. degree from the Nanyang Technological University, Singapore, in 2017. He is currently pursuing Ph.D degree in the School of Electrical & Electronic Engineering from Nanyang Technological University.

His research interest includes photoacoustic/thermoacoustic for non-destructive sensing and imaging.

Song Yong Phua, Kelvin received the B.Eng. degree from the National University of Singapore, Singapore, in 2017. He is a Senior Engineer with the SMRT Trains Pte Ltd, Singapore.

Christian Ivan received the B.Eng. degree from the National University of Singapore, Singapore, in 2013. From 2014 to 2016, he was a Senior Engineer with the SMRT Trains Pte Ltd, Singapore. Since 2016, he has been a Manager at Permanent Way from the SMRT Trains Pte Ltd, Singapore.



Kye Yak See (SM'02) received the B.Eng. degree from the National University of Singapore, Singapore, in 1986, and the Ph.D degree from Imperial College London, U.K., in 1997.

From 1986 to 1991, he was a Senior Engineer with Singapore Technologies Electronics, Singapore. From 1991 to 1994, he was a Lead Design Engineer with ASTEC Custom Power, Singapore. Since 1997, he has been a Faculty Member with Nanyang Technological University, Singapore, where he is currently an Associate Professor with the School of

Electrical and Electronic Engineering. He holds concurrent appointment as the Director of the Electromagnetic Effects Research Laboratory, Singapore, and the SMRT-NTU Smart Urban Rail Corporate Laboratory, Singapore. His current research interests include electromagnetic compatibility (EMC), signal integrity, and real-time condition monitoring.

Dr. See was the Founding Chair of the IEEE EMC Chapter, the IEEE Aerospace and Electronic Systems Society, and the IEEE Geoscience and Remote Sensing Joint Chapter in Singapore. He was the Organizing Committee Chair of the 2006 EMC Zurich Symposium and the 2008 Asia-Pacific EMC Conference and the General Chair of the 2015 Asia-Pacific Conference on Synthetic Aperture Radar. Since 2012, he has been the Technical Editor of IEEE Electromagnetic Compatibility Magazine.



Yuanjin Zheng (SM'06) received the B.Eng. and M.Eng. degrees from Xi'an Jiaotong University, Xi'an, China, in 1993 and 1996, respectively, and the Ph.D. degree from Nanyang Technological University, Singapore, in 2001.

From July 1996 to April 1998, he was with the National Key Laboratory of Optical Communication Technology, University of Electronic Science and Technology of China. In 2001, he joined the Institute of Microelectronics (IME), Agency for Science, Technology and Research (A*STAR), and had been a principle investigator and group leader. In July 2009, he joined the Nanyang Technological University, and now as an associate professor and program directors. His research interests are integrated circuits design, 3D imaging and display, and SAW/BAW/MEMS sensors for NDT etc. He has authored or coauthored over 300 international journal and conference papers, 22 patents filed, and 5 book chapters. He has led and completed projects by working with industry partners and developing commercial products.

Corporate Membership

The EMC Society offers Membership to organisations. We would like to take this opportunity to recognise our Corporate Members.

- EMC Technologies, www.emctech.com.au
- Fuseco Power Solutions, www.fuseco.com.au
- Department of Defence, Accredited Test Services
- Compliance Engineering, www.compeng.com.au



Electromagnetic Compatibility Society of Australia

For engineers concerned with electromagnetic compatibility and technological safety.

Standards Update

IEC Recently Published

CISPR TR 16-4-4:2007+AMD1:2017+AMD2:2020 CSV

Specification for radio disturbance and immunity measuring apparatus and methods - Part 4-4: Uncertainties, statistics and limit modelling - Statistics of complaints and a model for the calculation of limits for the protection of radio services

CISPR TR 16-4-4:2007+AMD1:2017+AMD2:2020 contains a recommendation on how to deal with statistics of radio interference complaints. Furthermore it describes the calculation of limits for disturbance field strength and voltage for the measurement on a test site based on models for the distribution of disturbances by radiated and conducted coupling. This second edition of CISPR 16-4-4 contains two thoroughly updated Clauses 4 and 5, compared with its first edition. It also contains, in its new Annex A, values of the classical CISPR mains decoupling factor which were determined by measurements in real low-voltage AC mains grids in the 1960s respectively. This consolidated version consists of the second edition (2007), its amendment 1 (2017) and its amendment 2 (2020). Therefore, no need to order amendment in addition to this publication.

STANDARDS AUSTRALIA – CEO REPORT

Australia continues to respond to the challenges of COVID-19, with many industries and community sectors managing massive disruption. At Standards Australia we have worked quickly at facilitating standards development remotely and adapting our processes so we can continue our core business of supporting industry, government and the wider Australian community.

The resilience and cooperation exhibited by the Australian people at the beginning of 2020 while responding to the bushfire crisis is again on show as we face this next challenge. It is encouraging to see so many Australian businesses and public sector organisations respond quickly to address urgent requirements of the health care sector.

Factories once making high-end clothing are now developing face masks and companies once making gin are now shifting to manufacturing hand sanitiser. To support this effort, earlier this month we released directory material for Australian manufacturers; this document is intended to help manufacturers



find information on relevant standards, such as respiratory protection, surgical masks and gloves, quickly and effectively.

This month we also supported the #flattenthecurvehack, an exciting event in which teams brainstormed and developed solutions to the COVID-19 crisis. Winners included a 3D-printed adjustable face-shield and a new platform called 'Class Party' which provides a virtual reality learning experience for school children learning from home.

Hopefully, many of the ideas and solutions that came out of the event will be able to assist Australia and the world deal with current challenges. The #flattenthecurvehack is another instance of individuals and organisations working together and thinking outside the square to achieve practicable outcomes during this crisis – we are proud to have been involved.

In conjunction with continued standards development and collaboration across our thirteen sectors, the directory material and hackathon are just two examples of the different solutions and initiatives Standards Australia has actioned in an effort to effectively support industry, government and individuals during the COVID-19 crisis.

While we adjust to this new reality as a nation, Standards Australia is committed to continued productivity and effectiveness. I look forward to working with many of you in the months to come as we search for innovative solutions to the challenges 2020 is presenting.

Adrian O'Connell,
Chief Executive

Updated international radiation safety guidelines

From ARPANSA

ARPANSA maintains the safety standard for radiofrequency electromagnetic energy – also known as radio waves. Radio waves are produced from various sources including mobile telecommunications, radio, television and Wi-Fi. Our safety standard is based on guidelines published by the International Commission on Non-ionizing Radiation Protection (ICNIRP) and relied on by the World Health Organization (WHO). ICNIRP has recently released a revision of its guidelines for radiofrequency radiation protection. The 2020 ICNIRP guidelines are an update of the previous 1998 guidelines and include a detailed explanation of how exposure limits have been set, along with a review of current research into radio waves and health. The exposure limits set in the updated guidelines are similar to those in the 1998 guidelines, with some refinements. These refinements take into account modern measurement practices and advances in modelling based on relevant research. ‘The level of protection provided by our current standard is comparable to that provided by the new ICNIRP guidelines’, said Dr Carl-Magnus

Larsson, ARPANSA CEO. ‘It is reassuring to see the scientific consensus continues to support current standards, which provide strong public protection’.

The refined ICNIRP guidelines have triggered a review and update of ARPANSA’s radiofrequency standard. The volume of research and scientific evidence underpinning these new guidelines has increased substantially since the previous edition. It is important that this evidence, along with advances in measurement and modelling is addressed in our revised standard.

ARPANSA’s standard for radio waves: Radiation Protection Standard for Maximum Exposure Levels to Radiofrequency Fields - 3 kHz to 300 GHz (2002) (RPS3 Link Below) will be updated during 2020 to ensure alignment with the new ICNIRP guidelines. ‘We look forward to sharing our new draft for public consultation later in the year’, said Dr Larsson.

View the updated ICNIRP guidelines: <https://www.icnirp.org/en/activities/news/news-article/rf-guidelines-2020-published.html>. Differences between the ICNIRP (2020) and previous guidelines <https://www.icnirp.org/en/differences.html>. ARPANSA RPS3 <https://www.arpansa.gov.au/regulation-and-licensing/regulatory-publications/radiation-protection-series/codes-and-standards/rps3>.

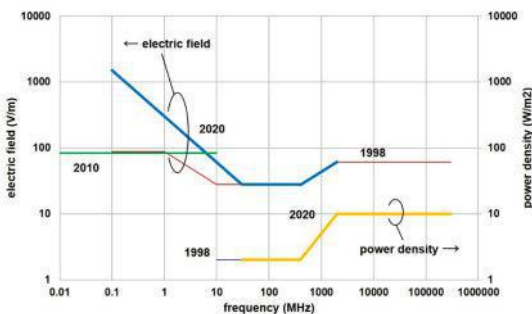


Figure 1. Whole body average reference levels for the general public for the ICNIRP (1998), ICNIRP (2010) and ICNIRP (2020) guidelines, for the 100 kHz to 300 GHz frequency range. Note that the units of the two y-axes (i.e. electric field and power density) are independent of each other.

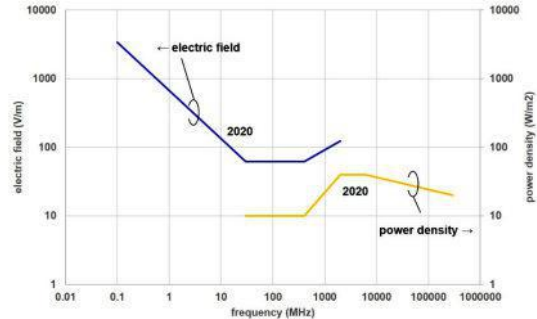


Figure 2. Reference levels for the general public applying to local exposures ≥ 6 min for the ICNIRP (2020) guidelines, for the 100 kHz to 300 GHz frequency range. Local exposure reference levels were not given in the ICNIRP (1998) and ICNIRP (2010) guidelines. Note that the units of the two y-axes (i.e. electric field and power density) are independent of each other.

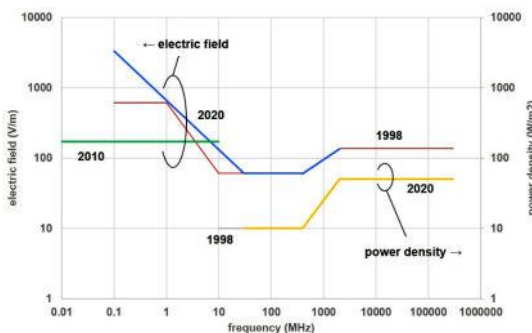


Figure 3. Whole body average reference levels for workers for the ICNIRP (1998), ICNIRP (2010) and ICNIRP (2020) guidelines, for the 100 kHz to 300 GHz frequency range. Note that the units of the two y-axes (i.e. electric field and power density) are independent of each other.

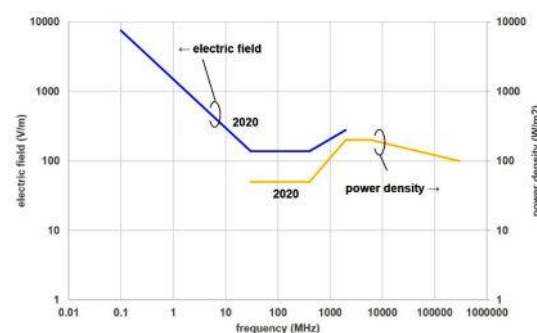


Figure 4. Reference levels for workers applying to local exposures ≥ 6 min for the ICNIRP (2020) guidelines, for the 100 kHz to 300 GHz frequency range. Local exposure reference levels were not given in the ICNIRP (1998) and ICNIRP (2010) guidelines. Note that the units of the two y-axes (i.e. electric field and power density) are independent of each other.

- Current version is Edition 9 of May 2018
- Editorial revision and restructure using a more technology independent approach. The term 'module' used instead of 'independent auxiliary'. Three basic ports: 'wired network'; 'local wired'; and, 'enclosure'.
- Maximum frequency extended to 1GHz.
- Annex A insertion loss requirement deleted.
- New requirement for GU10 self ballasted lamp.
- Addition of the common mode current probe test method for various ports (in addition to voltage measurement).
- Introduced limits for magnetic field measurements at 3 metres as an alternative to Large Loop Antenna System (LLAS) where the DUT doesn't fit within the LLAS.
- Introduced CDNE (Coupling Decoupling Network for measuring Emissions) method up to 300MHz where the highest internal frequency is below 30MHz and the DUT is smaller than 3m x 1m x 1m.
- Measurement Instrument Uncertainty (MIU) fully implemented.
- Measurement of Power Spectrum Density (PSD) mask as per ITU as an alternative to AAN port measurements on telecommunications ports.
- Introduction of RMS-Average detector as an alternative to Quasi-Peak and CISPR Average.
- Add provisions for multimedia equipment with Wireless Power Transfer.
- Increased test method controls for cables leaving the test volume (VHF-LISN).
- Measurement method and limits for above 1GHz; may require a full planar antenna scan (no tilt) from 1m to 4m.
- Colour bar test pattern clarification.

CISPR 32 – Multimedia equipment

Current version is Edition 2 of 31 March 2015

- For average limits given in CISPR 32 the correct detector is the CISPR Average Detector
- Adds outdoor units of home satellite receivers (Low Noise Block).
- Fully Anechoic Room added for measurements below 1GHz.
- Emission test arrangements for DUTs with multiple possible configurations: floor standing, wall mounted, table top, to be tested as table top only.
- Annexes for pre-compliance testing using TEM waveguide and RVC added.
- Expected in Amendments to Edition 2 or Edition 3